

SPACECRAFT ORBIT DETERMINATION ENHANCEMENT BY USING LOW-ALTITUDE PLANETARY OPTICAL IMAGES

Davide Silvestri⁽¹⁾, Alessandro Bevilacqua⁽²⁾, Alessandro Gherardi⁽²⁾, Paolo Tortora⁽¹⁾

⁽¹⁾ *University of Bologna, DIN, Via Fontanelle 40, I-47121, Forlì, Italy, +39 0543 374439, d.silvestri@unibo.it, paolo.tortora@unibo.it*

⁽²⁾ *University of Bologna, ARCES, Via Toffano 2/2, I-40125, Bologna, Italy, +39 051 2095409 agherardi@arces.unibo.it, alessandro.bevilacqua@unibo.it*

Abstract: *A novel technique for trajectory determination of planetary orbiters by using optical images of the planetary surfaces, in addition to standard radiometric observables, is proposed and tested with some preliminary results. The methodology is based on relating two sequential views of the same scene of the planetary surface in a mathematical form exploiting fundamentals of homographic projections. The characteristic features selected in sampled images and used in the described method are corner points. These features are matched between two sequential views of the same scene of the planetary surface sampled by the camera. In order to test the feasibility of this method, a simulation framework is developed: it allows to generate synthetic images of the planet surface according to the orbiter position and orientation. A synthetic Digital Elevation Model (DEM) is generated and rendered by a ray tracing software according to the orbiter pose and camera parameters. The pattern matching algorithm is then applied to the generated high resolution images to test the proposed method in a realistic scenario. Preliminary results are presented by means of a simple orbital model implementation where the main geometries and constraints of BepiColombo's Mercury Planetary Orbiter are taken in account, and simulated Doppler and optical observables are used in a simplified scenario.*

Keywords: *Trajectory determination, planetary images, orbiter spacecraft, satellite imaging, pattern matching*

1. Introduction

An analysis of performances of a novel technique for spacecraft navigation is shown, where optical information is extracted from planetary images of an orbiter spacecraft in a low computational way. The optical observables are expressed mathematically relating two successive views of the same surface area, resulting in a mark-less formulation exploited using Corner point features. The addition of landmarks to the estimated parameters is avoided, thus reducing the degradation of the orbit determination process and simplifying the modularity as a plug-in to be integrated into existing spacecraft navigation software.

In Section 2 the image synthesis, corner point extraction and matching is described, showing the capabilities of the simulator. In Section 3 the proposed optical observables and their partial derivatives are expressed. Next, a sensitivity analysis is carried out on the observables as a function of gravitational harmonics and planetary rotation parameters and finally results of an Extended Kalman Filter implementation are shown in Section 4.

As the simulation requires a set of underlying assumptions and parameters to select, we used the MPO spacecraft of the BepiColombo mission to Mercury as a reference scenario. This is an orbiter spacecraft with an on-board optical system called SIMBIO-SYS, comprising a narrow angle high resolution channel (HRIC) whose parameters will be the ones used in the following

analysis. The orbiter will operate in a polar orbit of 400km of altitude at perihelion and 1500km at aphelion. This orbital geometry will be used as the main one for all simulations.

2. Image synthesis and elaboration

The lack of high resolution images of the Mercury surface taken at different illumination conditions requires to operate through simulations. We therefore setup a simulation environment built to generate synthetically all the necessary images. The S/W simulator developed by the Computer Vision Group (CVG) of DEIS, is capable of generating on demand synthetic images of the surface of Mercury for the analysis of the performance of a navigation algorithm for the orbiter spacecraft.

In the following, the current capabilities of the software in terms of state-of-the-art image generation and processing is presented.

2.1. Synthetic images

The simulation system builds a Digital Elevation Model (DEM) of the Mercury surface by simulating a set of impact craters on an initial terrain model. Craters are randomly distributed on the surface according to a set of parameters defining their diameters and the density distributions. Each crater is modeled by combining impact crater models [7,8,9] and surface fractal details. Mercury presents mainly two types of craters: simple craters, bowl-shaped structures formed by the smallest impact bodies which create sharp rims, and complex craters, characterized by terraced walls due to subsurface faults which present a central peak of material brought up from beneath the surface. The transition diameter between simple and complex crater is 10.3 km according to [9].

We modeled the craters by using Gaussian shapes. A number of slightly shifted 3D Gaussian shapes have been superimposed in order to obtain an irregular border on top of the crater (see Fig. 1). These shapes have been cut starting from an arbitrary base level (chosen by a random component). The inner side of the crater has been modeled by reversing each Gaussian shape, after doubling its sigma, in order to simulate a smooth impact area. Complex craters have been also modeled by superimposing a central peak in the impact area.

The synthetic image generation procedure is outlined as follows:

1. a fractional Brownian motion (fBm) algorithm generates the plain surface according to a $1/f^n$ pink noise, where f is the frequency and n the argument. This procedure allows to define the coarser texture level free from any other feature (i.e., craters, bumps, scratch, etc...) at each scale;
2. a random number of craters is added to the surface, with variable diameter size according to the parameters given;
3. step 1 and 2 are repeated a prefixed number of times for each scale, until the resulting DEM is generated.

The first step allows to generate the main coarser irregular surface, and at each iteration it smooths the previous generated DEM in order to simulate different ages of impacts on the surface. This behavior is carried out by increasing the argument of the pink noise, at each scale, where a number of craters is then randomly added.

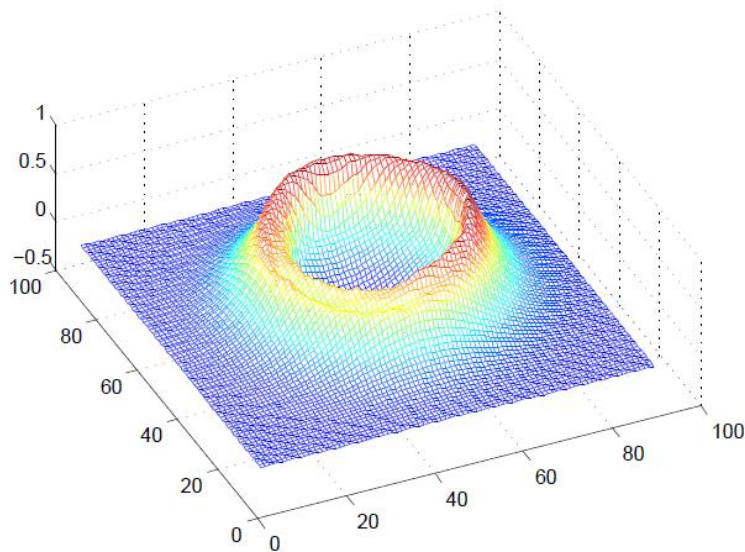


Figure 1 Simulated crater

The final DEM is further ray-traced to generate synthetic images (Fig. 2) according to the given altitude of the spacecraft and to the Sun azimuth and elevation angles.

2.2. Dataset

A first campaign was undertaken with some main assumptions for the generation of synthetic images:

- Only one DEM for the target area is used for the generation of the images
- The resulting image generated from the synthetic DEM is obtained with a nadir pointed camera with constant depth equal to 845 km, at this altitude the ground resolution will be about 10.6 m/pixel for the MPO HRIC.

A requirement for a good pattern matching without ill-conditioning is the size of the overlapping area, selected in this scenario as a square with side of 512 pixel (conservative)[4].

The following illumination conditions were selected for the evaluation of shadowing at high latitude:

- 18 images with Sun Elevation=5° and Az $\in [0,5,\dots,90]^\circ$
- 18 images with Sun Elevation=2° and Az $\in [0,5,\dots,90]^\circ$

This illumination variation in Azimuth is 5 times higher than what expected for MPO, thus providing a highly conservative condition [4].

2.3. Corner Points Extraction and Pattern matching

The Matlab® computer vision toolbox was used in this phase where corner points are detected by means of the Minimum value Shi & Tomasi corner detector.

The Matlab® *matchFeature* function was selected for this task, providing the features most likely to correspond and whose strongest matches are selected for the evaluation of the translation. Almost an exact matching is reached, as a consequence of the lacking of optical

deformation models and a subtle time varying noise present in the camera hardware chain. The addition of those effects is currently in phase of implementation.

Capabilities of enhancement and reduction of the area of pattern matching (variable overlap as a function of images sampling time) and shape are implemented for future use as shown in Figure 2.

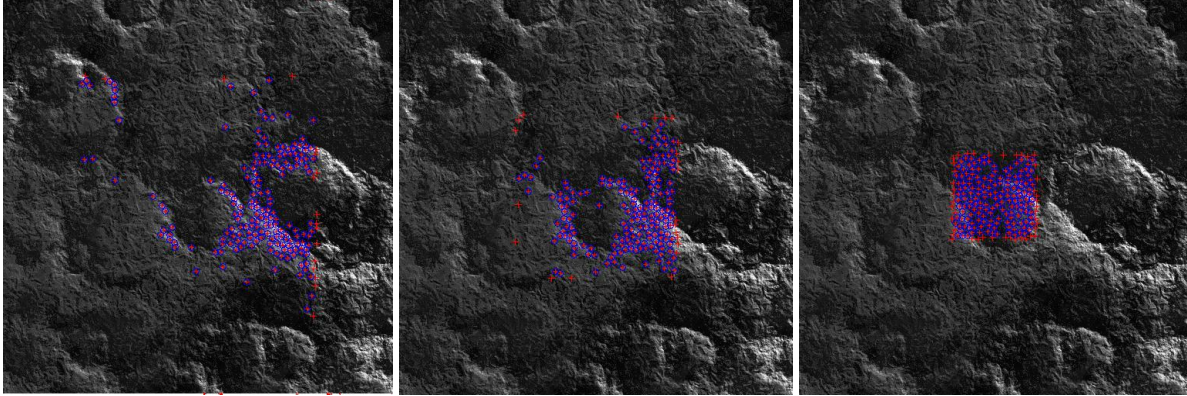


Figure 2 Variable simulated overlap for an image pair

3. Optical observables

This Section describes the mathematical formulation of the optical information in such a way they are easily processed by a computer. An analysis of the effects of wrong gravitational and rotational models on the observables is presented and operational and technical aspect of the methodology are discussed together with the estimation algorithm implemented.

3.1 Mathematical formulation

The main model used is the pinhole camera model, describing the relation between the image plane of the camera and the 3D scene from a camera-centric reference frame (C.r.f.) in Eq. 1.

$$\lambda_i z_i = \mathbf{K} \mathbf{R}_i [\mathbf{r}_i^{\text{CP}} - \mathbf{M}_i \mathbf{X}_i^{\text{S/C}}] \quad (1)$$

Where λ is a scale factor, r is the vector representing the 3D observed positional coordinates in the camera reference system and z is the projection in the image plane of the point r , transformed by means of the intrinsic parameters \mathbf{K} and the extrinsic parameters \mathbf{R} and \mathbf{X} . The index i refers to the sampling time t_i . \mathbf{R}_i is the rotational matrix from a planet-fixed reference frame (P.r.f.) to the C.r.f. and \mathbf{M}_i is the rotation matrix from an inertial to a P.r.f. and finally the \mathbf{X} position vector is the position of the camera center in an inertial reference frame (considered coincident for hypothesis with the S/C reference frame). Additional information on the mathematical modeling used here can be found in [2].

It is possible to express the r coordinates (defined in a P.r.f., hence constant in time), in a different view acquired in a similar geometry but at a different time and replace this new equation in Eq. 1. The result is the observation equation Eq. 2.

$$z_i = \frac{\lambda_j}{\lambda_i} H_i^j z_j - \frac{1}{\lambda_i} \mathbf{K} \mathbf{R}_i [\mathbf{M}_i \mathbf{X}_i^{S/C} - \mathbf{M}_j \mathbf{X}_j^{S/C}] \quad (2)$$

Where the linear Homography matrix H_i^j is defined in Eq. 3

$$H_i^j = \mathbf{K} \mathbf{R}_i \mathbf{R}_j^{-1} \mathbf{K}^{-1} \quad (3)$$

The time between two acquisitions is called sampling time $\Delta t_i^j = t_i - t_j$.

For hypothesis the scale factor ratio is considered equal to one as, at first approximation this equation is not so sensitive to slow changes in line of sight distances. This is even more true for very short sampling time intervals and when no orbital manoeuvres (change in semi major axis) are introduced in-between this interval.

The scale factor is usually defined as the z coordinate in the C.r.f. of the 3D observed point:

$$\lambda_i = \mathbf{R}_i^T(:,3) [\mathbf{r}_i - \mathbf{M}_i \mathbf{X}_i^{S/C}] \quad (4)$$

The nonlinear term is sometimes called the parallax shift term and conveys the following problem represented in Eq. 6: dividing the error contributions in the state estimate in a constant and a variable part,

$$\mathbf{X}_i^{S/C} - \hat{\mathbf{X}}_i^{S/C} = \boldsymbol{\varepsilon}_i^{S/C} \quad (5)$$

$$\mathbf{X}_j^{S/C} - \hat{\mathbf{X}}_j^{S/C} = \boldsymbol{\varepsilon}_{\text{Con}}^{S/C} \quad (6)$$

And

$$z_i - \hat{z}_i = -\frac{1}{\lambda_i} \mathbf{K} \mathbf{R}_i [\mathbf{M}_i \boldsymbol{\varepsilon}_i^{S/C}] \quad (7)$$

The constant part of the estimation error is not observed in the residuals, hence cannot be estimated, but it has to be considered (otherwise a non-conservative estimate will be carried out). The consequence is that a good knowledge of the state at epoch is required, and in this way we can maintain the orbit, by nullifying the drifting part of the propagation error.

The only way to observe the constant part of the error is through the use of an absolute method employing geometrical features.

The partial derivatives of the measurement equation are formulated in Eq. 7 only with respect to the position because they are all zero with respect to velocity at epoch.

$$\frac{\partial z_i}{\partial X_i^{S/C}} = -\frac{\lambda_j}{\lambda_i^2} \frac{\partial \lambda_i}{\partial X_i^{S/C}} H_i^j z_j + \frac{1}{\lambda_i^2} \frac{\partial \lambda_i}{\partial X_i^{S/C}} KR_i [M_i X_i^{S/C} - M_j X_j^{S/C}] - \frac{1}{\lambda_i} KR_i M_i \quad (8)$$

$$\frac{\partial \lambda_i}{\partial X_i^{S/C}} = -R_i^T(:,3) M_i \quad (9)$$

Derivatives with respect to state and observables at time t_j are null because a reference position is required to infer variations at another point. Then $\frac{\partial z_j}{\partial X_i^{S/C}} = 0$, $\frac{\partial \lambda_j}{\partial X_i^{S/C}} = 0$ and $\frac{\partial X_j^{S/C}}{\partial X_i^{S/C}} = 0$.

3.2 Sensitivity analysis

In this section the sensitivity of the defined optical observables with respect to different parameters is investigated. This step is fundamental for the design phase of the filter, to understand the requirements in terms of model requirements and possibly for the addition of parameters whose uncertainty shall be taken in consideration in the estimation process.

3.2.1. Rotational parameters

The first part of the sensitivity analysis concerns the rotational parameters. In simulations, the main considered model is the Mercury IAU 2000 Model, meanwhile in estimation a custom model is implemented, and the main coefficients used for the simulation are reported here for clarity. Only Length-of-Day harmonics are evaluated.

$$W = W_0 + W_1 \sin(M1) - W_2 \sin(M2) - W_3 \sin(M3) - W_4 \sin(M4) - W_5 \sin(M5) \quad (10)$$

Analyzed cases:

- Case 1: validation between a 6 parameters model and the IAU 2000 Model
M1=M2=M3=M4=M5=0
- Case 2: comparison between a 6 parameters model and the IAU 2000 Model with M1≠0,
M2≠0, M3=M4=M5=0
- Case 3: comparison between a 6 parameters model and the IAU 2000 Model

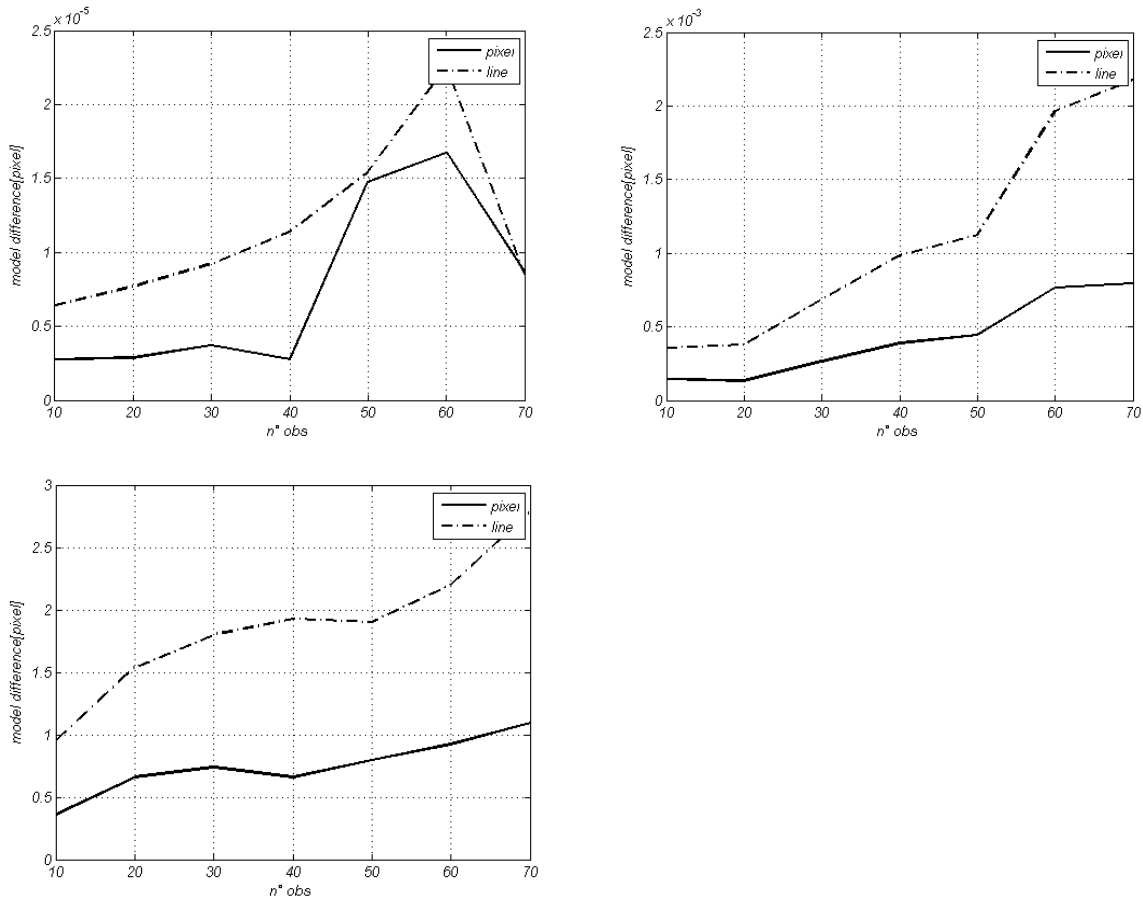


Figure 3 Optical observables sensitivity to the planetary rotational model. Cases 1, 2, 3

The simulation is carried out analyzing a set of observables sampled nearly once a day. Case 1 is only a validation and provides the lower bound dependent substantially on optical noise. In Case 2 we have still good matching remaining well under the level of pattern matching resolution. Case 3 highlights some sensitivity problems where a peak of 3 pixel of deviation is reached. In conclusion an arc of nearly 70 days with this navigation method should be exploited with the need of a knowledge of the rotational parameters above the classical 6 parameters one, or with the integration of consider parameters in the filter providing informations about the uncertainty of rotational parameters, exploiting partial derivatives of the optical observables with respect to rotational parameters.

3.2.2. Gravitational harmonics

As no gravitational harmonics are currently available in the PDS, we decided to use Mars gravitational harmonics and scaling them using Mercury's GM and radius in preparation to the Messenger mission expected data.

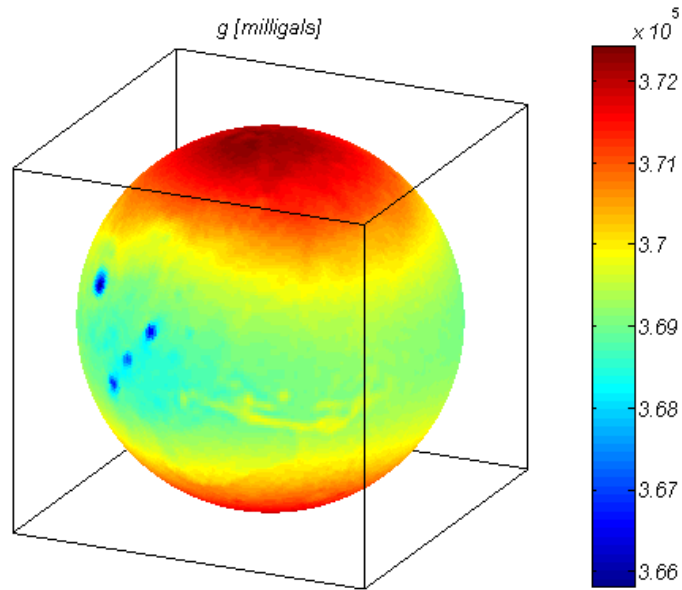


Figure 4 Mars gravity field

Zonal harmonics are not treated because ground track move substantially on a line of constant zonal potential. Sectorial and Tesseral harmonics are treated in the following cases:

- CASE 1: validation using the same model in simulation and estimation
- CASE 2: zonal and tesseral harmonics knowledge in estimation with $l=0$, $m=0$, simulation model with $l=6$ $m=6$
- CASE 3: zonal and tesseral harmonics knowledge in estimation with $l \leq 4$, $m \leq 4$, simulation model with $l=6$ $m=6$
- CASE 4: zonal and tesseral harmonics knowledge in estimation with $l \leq 5$, $m \leq 5$, simulation model with $l=6$ $m=6$

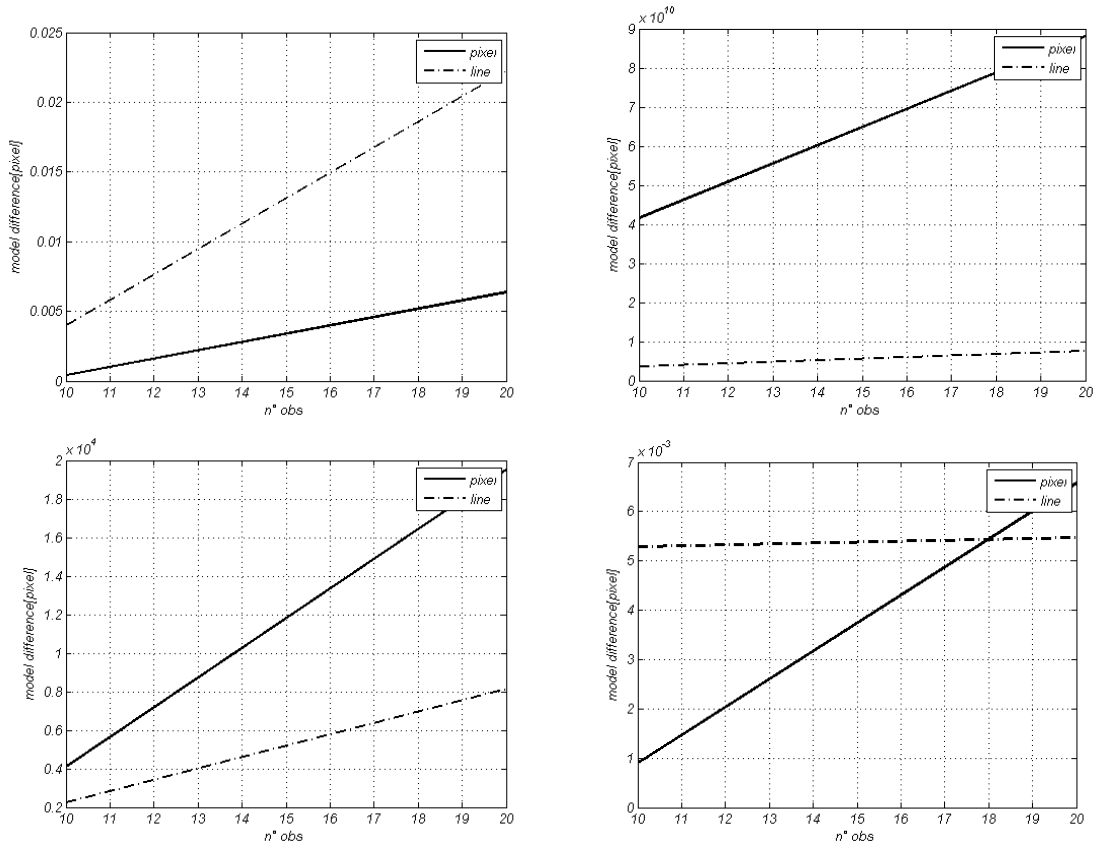


Figure 5 Optical observables sensitivity to the gravitational model. Case 1, 2, 3,4

Figure 5 can only highlight a qualitative behavior as we have not implemented the real Mercury gravitational model, and perturbations may be different from those in an Hermean scenario but it is clear that also gravitational harmonics may produce considerable effects mostly at low degrees.

As a consequence of the sensitivity analysis we should take in consideration the effect of uncertainty in gravitational harmonics and rotational parameters if the knowledge is not high enough. This statement strongly depends on the shape of the orbiting body, and partitioning the parameters vector in “solve-for” and “consider” parameters can be taken into account.

A first conclusion is that the proposed trajectory determination enhancement methodology could not be effective in the case of S/C orbiting asteroids because of the very inhomogeneous shape of the body and uncertain gravity, which would require the use of database-based methodologies.

3.3. Image acquisition plan

The overlap between two images is represented in Figure 6. Only the boxes with blue borders are downloaded to Earth instead of the full images. Uncertainty in the S/C pointing has to be considered in an operational phase (resulting in an larger sub-area of the image to be downloaded).

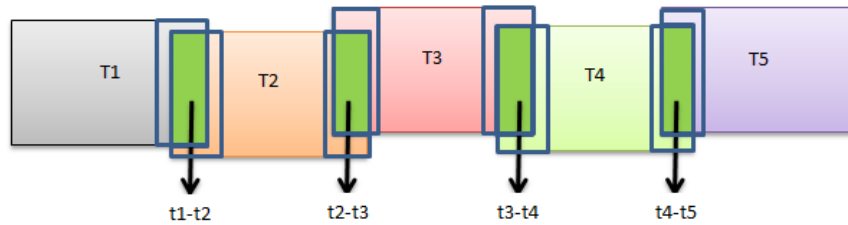


Figure 6 Schematic example of a set of five sequentially sampled images with four overlapping regions.

The synthetic images will be produced with no attitude pointing error. The camera observer will be then nadir pointing. The attitude errors will be superimposed during the preprocessing. It is important to highlight that an Attitude Pointing Error (APE) is equivalent to the request of a larger image, indeed if we suppose an APE of $102''$ in one direction and in the following image the same APE in the opposite direction, the total effect will be $204''$ equivalent to an image shift of about 100 pixels.

From an operational point of view, it is of interest to evaluate the required throughput of this methodology in terms of downloaded data, which is mainly due to the overlap between a pair of images.

In the following we will estimate the minimum required image dimensions and the consequent effects on the throughput with a square image, to highlight that a strip image with the smaller side parallel to the Along-Track direction will reduce the constraint on the sampling time computed above, therefore the condition of square image is not a constraint.

Selecting as a constraint to have at least 5% of a full image for ill-conditioning avoidance, we obtain that from an HRIC image of 4.19Megapixel (2048x2048), a square sub-image of 458x458 pixels is enough.

If each pixel is defined in b/w by 14bit, an Image dimension of 7.3 Mbytes (the images will be also compressed in jpeg format, so, this value is highly conservative) is obtained and a subset of 5% of the image dimension is about 0.37Mbytes.

In a 80d window, 160 images are produced if the sample time is, for example, 0.5d. Therefore we produce 60 Mega Byte each 80d window. This value is negligible with respect to the scientific return that is a Total downlink= 1550 Gb/y.

Furthermore with an on-board corner point extractor, we should download not the entire overlapped sub-image but only a set of 2D image coordinates with a certain set of characteristics defined apriori, reducing the throughput of the methodology from Megabytes to kilobytes, e.g. 2 bytes for each corner point, for a set of 500/1000 corner points per image to be conservative.

3.4. Navigation algorithm

In this section the navigation algorithm is described, with emphasis on the special efforts done to obtain something very similar to an operational system.

At first an orbital integrator generate a simulated orbit used for the schedule of epochs satisfying special requirements for the generation of optical observables, i.e. the constraint of overlapping. Therefore the maximum sampling time is indirectly computed as a function of the input body-fixed latitude position where images are acquired. Those epochs are associated with a set of images generated by the CVG Team of DEIS as described in Section 2, with a sweeping illumination in Sun azimuth and with a fixed elevation, in the MPO scenario, the main result is a

set of images with very long shadows sweeping around craters and very low illumination conditions. Afterwards corner points extraction and pattern matching is done to obtain a realistic pattern matching error. The reference image is supposed to be the image acquired at time t_i and in the illumination coordinate system $(Az, El)_i$ while the other image is acquired with a certain coordinate $(Az, El)_{i+1}$ at time t_{i+1} . A first hypothesis is that the first image is the real output from the camera at time t_i with the right attitude and position. Optical deformations due to thermal effects and defects and hardware time varying noise can be applied sequentially to this synthetic image simulating the optical channel followed by the hardware chain.

The second image is the one acquired at t_{i+1} but viewed with the conditions of time t_i , therefore a nonlinear Homography transformation must be applied.

After this transformation it is possible to switch to the subspace of corner point features, detected with the methodology defined by Shi&Tomasi.

We can now test the simulation part projecting CPs of the image at time t_i to time t_{i+1} . In this way the pattern matching will be facilitated because of the reduced relative rotation and shift. In the MPO scenario, also an image transformation composed by a translation and a rotation is adequate because of the narrowness of the field-of-view of HRIC and the reduced altitude of the S/C but for a matter of generality we have considered all possible subtle transformations, i.e. orthographic projections.

The attitude is computed in parallel to the simulation phase and provided as a ground-truth to the estimator as in an operational navigation phase. Hence, in simulations, thanks to the observations scheduler, it is possible to generate apriori the required set of camera attitude matrix with respect to an inertial reference frame and a body fixed reference frame augmented with AME error. It is highlighted that images will be affected by the AME errors also in the simulated scenario.

In the estimation phase the spacecraft estimated position at the required times t_i and t_{i+1} is produced by propagating the orbit, updated at time t_{i+1} with all previous observations, back to time t_i together with the state covariance matrix. With this pair of states we are capable of projecting the CPs of image at time t_i to time t_{i+1} and produce residuals with respect to the CPs at time t_{i+1} as a result from elaboration of the image at time t_{i+1} processed in the simulation. The residuals are therefore function of the spacecraft estimated position at epoch and the estimation process for navigation purposes is possible.

Finally, a statistical comparison of updated estimation residuals with respect to the one obtained in simulation will be carried out.

Note that the pattern matching with consequent outliers removal will be carried out only one time in simulation for each pair of images. In the estimation phase no tracking and labeling is still necessary. In an operative scenario the pattern matching will be done in estimation, but only one time for each pair.

3.4.1. Extended Kalman filter formulation

An Extended Kalman filter has been implemented for a qualitative evaluation of the performances of optical observables. Some modified equations are briefly reported highlighting the main structure of the filter.

In Equation 11, the Kalman gain is expressed in terms of apriori state error covariance P_i^- and as a function of partial derivatives of optical observables with respect to the estimated state G_i .

$$K_i = P_i^- G_i^T (G_i P_i^- G_i^T + C_i)^{-1} \quad (11)$$

$$C_i = R_i + H_i^j R_j (H_i^j)^T + \frac{\partial z_i}{\partial X_j^{S/C}} P_j \left(\frac{\partial z_i}{\partial X_j^{S/C}} \right)^T \quad (12)$$

R_i and R_j are the measurement noise matrix, one referred to the coordinates in the image plane of the second image of the pair, and one referred the other image of the pair. In Equation 12 a modified measurement noise matrix is shown, accounting for additional effects due to the relative formulation of the optical observables. It is a constraint linking two epochs where the constraint itself is free to move in the state-space due to the covariance associated at time t_i and at time t_j . The covariance matrix update is in the classical form of Equation 13.

$$P_i^+ = (I_6 - K_i G_i) P_i^- \quad (13)$$

The state transition matrix is computed for the propagation of the covariance matrix.

$$P_j = \Phi_j^i P_i^- (\Phi_j^i)^T \quad (14)$$

Where P_k^- is the error covariance matrix at the observable time, before the update. The same equations are applied for Doppler observables. Each type of observable is managed with a scheduler that process sequentially each observable when it comes available.

4. Results

In this Section the main results of the simulation are presented, showing a dead reckoning evaluation, i.e. the use of optical observables alone, and the complementarity between optical and radiometric data.

4.1. Dead reckoning solution

The observable is first used alone, from a starting epoch where the state is already known with good accuracy. We are applying a dead reckoning solution and it is expected that any potential divergence could occur over a long time span, but significantly reducing the effects of error propagation due to initial conditions. The clear weakness of this methodology results in a convergence to the initial condition error, because there is no possibility to infer the constant part of the error of the orbit, that is exactly the initial condition error at the starting position. We can conclude that when used alone, this optical observable keeps unvaried the initial error until propagation errors generated by the noise in the observables start degenerating the quality of the estimation. Optical observables are taken every half a day continuously. An initial condition with an error of tens of meters in position is provided, an attitude measurement error of 5'' (1- σ) and a pattern matching error of 0.1 pixel is selected. Additional considerations and analysis on the various types of errors affecting the described optical observables have been already analyzed elsewhere [4].

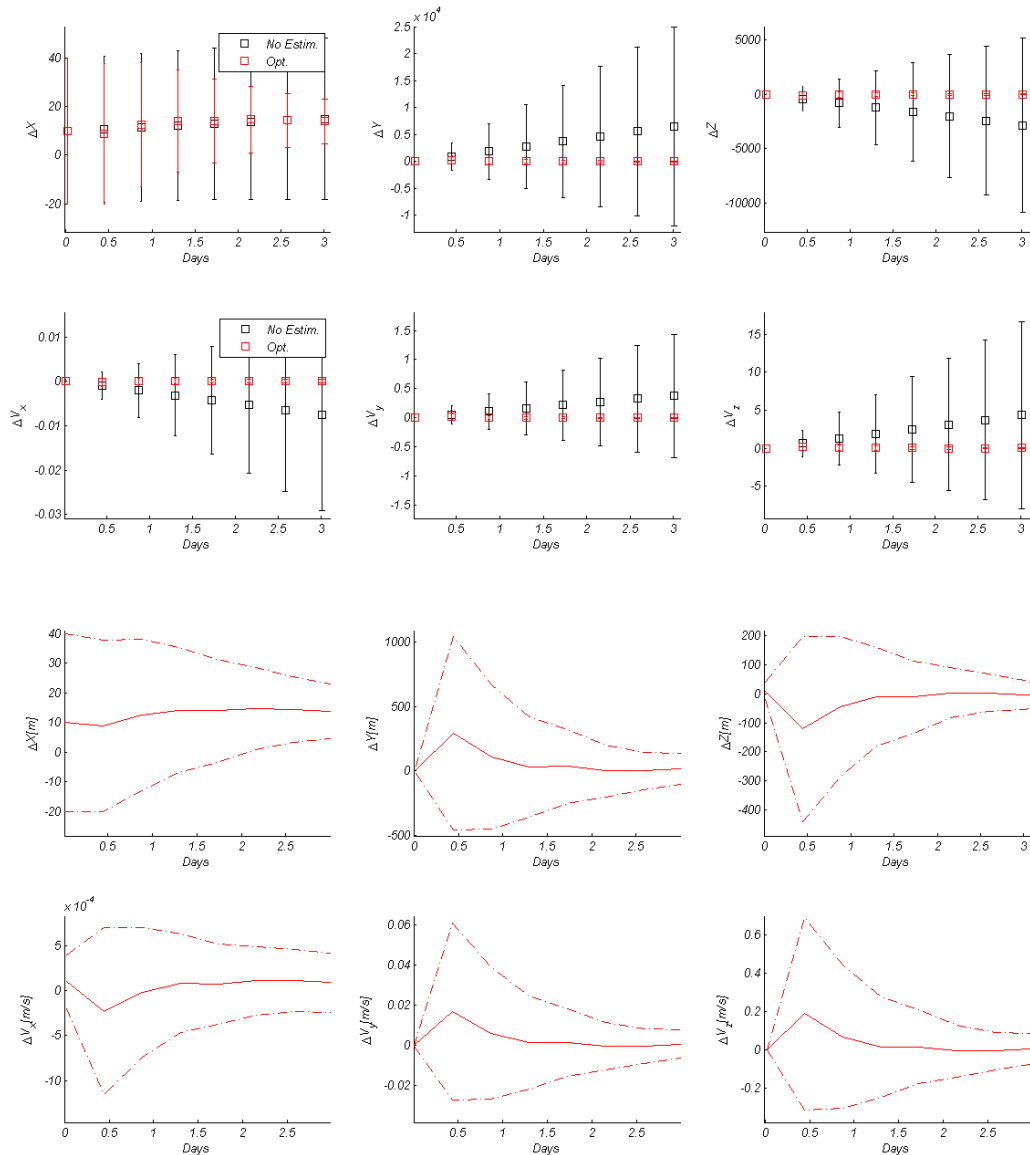


Figure 7 The first set of state parameters represents the propagation covariance with no estimation versus estimation with optical observables (the solid line represents the nominal value while the dash-dotted line represents the 3- σ deviation), the second set of state parameters zoom on optical estimation.

The first optical observation is generated half a day after the start of the navigation process because there is need to another sample at $t_i-0.5d$ to generate this observable, this lack of coverage is the cause of the initial divergence of the covariance of the state with time.

4.2. Weak direction evaluation

In this simulation, 8 hours of radiometric tracking are followed by 12 hours without radiometric data, meanwhile optical observables are taken every half a day continuously. An initial condition with an error of tens of meters in position is provided.

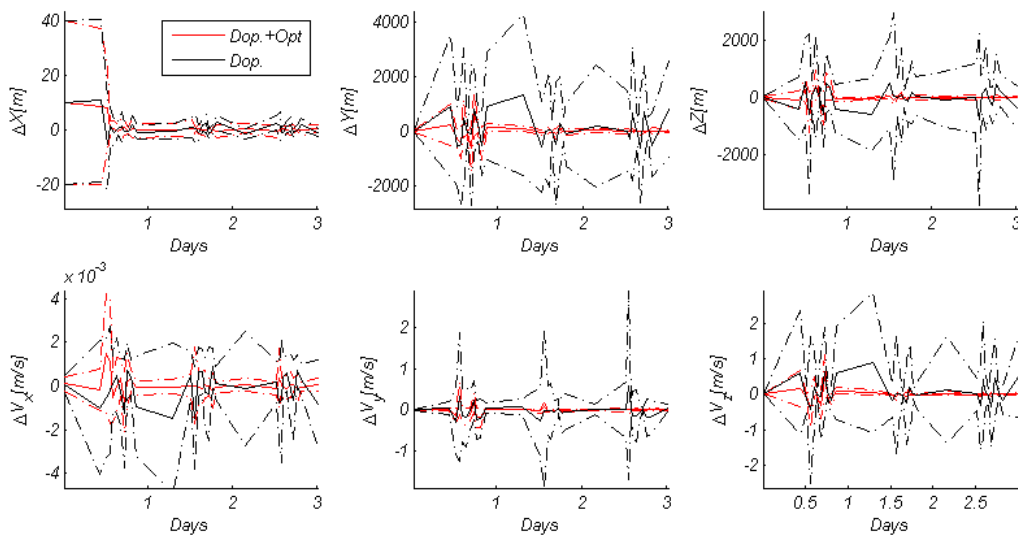


Figure 8 Orbital geometry condition with low Doppler sensitivity, covariance comparison between an estimation with Doppler observables alone (black line) and integration of Doppler and optical observables (red line), dash-dotted lines represent $3\text{-}\sigma$ bounds and solid lines the nominal value

There is a clear improvement in the estimation because the optical observables strongly contribute to provide informative content.

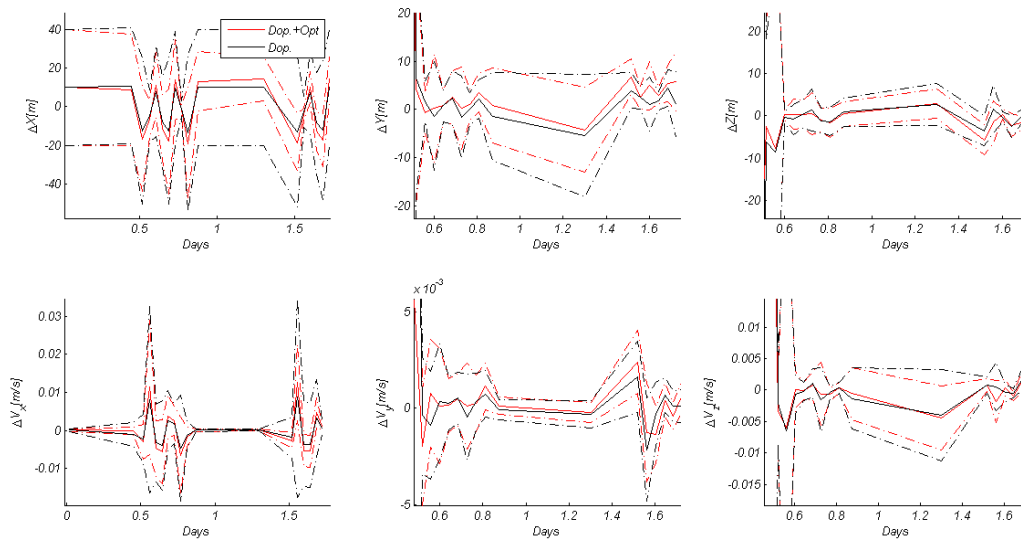


Figure 9 Orbit geometry condition with strong Doppler sensitivity, covariance comparison between an estimation with Doppler observables alone (black line) and integration of Doppler and optical observables (red line), dash-dotted lines represent $3\text{-}\sigma$ bounds and solid lines the nominal value

Optical observables in a classical configuration where Doppler observables have a strong informative content are of little use, as shown in Fig. 9. Additionally, in some cases they can degrade the estimation up to the level where the error bar does not including the zero value. This

effect should be reduced reiterating the estimation process, to reduce the apriori error and nominal value used at time t_j for each optical observable.

4.3. Future work

In the next future, the synthetic image generation and processing will be further expanded introducing all different error sources present in the camera and possible uncalibrated optical aberrations. Another main objective is the integration of the proposed estimation algorithm in the JPL Orbit Determination Program where optical observables will be processed in a batch way to improve the classical radiometric-based orbit determination. With this implementation it will be possible to validate the performances with very high reliability and obtain a fully integrated simulation environment. The integration of consider parameters, i.e. parameters whose value is not estimated but whose covariance is considered in the estimation will be undertaken, as a result of the sensitivity analysis carried out on the optical observables and presented in this paper.

5. References

- [1] Owen, W.M., Wang, T.C., (2010). NEAR Optical Navigation at Eros.
- [2] Bevilacqua, A., Bianchi, C., Carrozza, L., Gherardi, A., Melega, N., Modenini, D. & Tortora, P., (2010). Standalone Three-Axis Attitude Determination From Earth Images. *AAS 10-145*.
- [3] Tortora, P., Bevilacqua, A., Carrozza, L., Genova, A., Gherardi, A., Iess, L., Meriggiola, R., Palli, A., Palumbo, P., Zusi, M., (2011). Simulation of BepiColombo's Mercury Rotation Experiment. *EGU2011*, Vol. 13
- [4] Silvestri, D., Tortora, P., (2012), Enhancement of Trajectory Determination of Orbiter Spacecraft by using Planetary Optical Images, Conference Proceeding of ICATT, ESA/ESTEC, Noordwijk, Netherlands.
- [5] Coucaud, C., Kubota, T., Probabilistic motion estimation for near real-time navigation and landing on small celestial bodies.
- [6] Moyer, T., (2000), Mathematical formulation of the DPODP, Moyer, JPL technical report
- [7] Gault, D.E., Guest, J.E., Murray, J.B., Dzurisin, D., Malin, M.C. (1975): Some Comparisons of Impact Craters on Mercury and the Moon. *J. Geophys. Res.* 80(17), 2444–2460
- [8] Melosh, H.J., Ivanov, B.A. (1999), Impact Crater Collapse. *Earth Planet. Sci.* 27, 385–415
- [9] Pike, R.J.: In: Vilas, F., Chapman, C.R., Matthews, M.S. (eds.) *Mercury*, pp. 165–273. University of Arizona Press, Tucson (1988)